Received: 19 October 2017 | Revised: 15 February 2018 | Accepted: 18 February 2018

DOI: 10.1002/mrm.27176

FULL PAPER

Magnetic Resonance in Medicine

Single-shot spiral imaging at 7 T

Maria Engel[1] | Lars Kasper[1,2] | Christoph Barmet[1,3] | Thomas Schmid[1] | Laetitia Vionnet[1] | Bertram Wilm[1,3] | Klaas P. Pruessmann[1]

[1] Institute for Biomedical Engineering, ETH Zurich and University of Zurich, Zurich, Switzerland

[2] Translational Neuromodeling Unit, Institute for Biomedical Engineering, University of Zurich and ETH Zurich, Zurich, Switzerland

[3] Skope Magnetic Resonance Technologies AG, Zurich, Switzerland

Correspondence
Klaas P. Pruessmann, Institute for Biomedical Engineering, ETH Zurich and University of Zurich, ETZ F 89, Gloriastrasse 35, 8092 Zurich, Switzerland.
Email: pruessmann@biomed.ee.ethz.ch

Purpose: The purpose of this work is to explore the feasibility and performance of single-shot spiral MRI at 7 T, using an expanded signal model for reconstruction.

Methods: Gradient-echo brain imaging is performed on a 7 T system using high-resolution single-shot spiral readouts and half-shot spirals that perform dual-image acquisition after a single excitation. Image reconstruction is based on an expanded signal model including the encoding effects of coil sensitivity, static off-resonance, and magnetic field dynamics. The latter are recorded concurrently with image acquisition, using NMR field probes. The resulting image resolution is assessed by point spread function analysis.

Results: Single-shot spiral imaging is achieved at a nominal resolution of 0.8 mm, using spiral-out readouts of 53-ms duration. High depiction fidelity is achieved without conspicuous blurring or distortion. Effective resolutions are assessed as 0.8, 0.94, and 0.98 mm in CSF, gray matter and white matter, respectively. High image quality is also achieved with half-shot acquisition yielding image pairs at 1.5-mm resolution.

Conclusion: Use of an expanded signal model enables single-shot spiral imaging at 7 T with unprecedented image quality. Single-shot and half-shot spiral readouts deploy the sensitivity benefit of high field for rapid high-resolution imaging, particularly for functional MRI and arterial spin labeling.

KEYWORDS
algebraic image reconstruction, magnetic field monitoring, single-shot spiral, spiral imaging

1 | INTRODUCTION

Image encoding in MRI is performed with a large variety of strategies for traversing k-space. Among these, spiral readouts stand out in terms of time efficiency and average k-space speed, which can be achieved within given gradient amplitude and slew-rate constraints.[1–3] Single-shot spiral trajectories, in particular, rank among the fastest ways of covering k-space for given resolution and FOV.[4] Center-out spirals permit shorter TEs than echo-planar scanning and offer relative robustness against flow artifacts, as their first gradient moments are zero in the k-space center and continue to be nulled once per turn of the trajectory.[2,3,5] These properties render single-shot spiral acquisition attractive for a number of purposes, such as DWI,[6,7] arterial spin labeling (ASL),[8] and BOLD fMRI.[4,9] In fMRI, spiral readouts have even been used for acquisition of two images per shot, performing successive inward and outward spirals after a single excitation.[10,11]

However, to date, spiral readouts have not been widely deployed in applied studies for two primary reasons. First, spiral imaging is particularly sensitive to imperfections of

magnetic field dynamics, which give rise to blurring, distortion, and other artifacts when unaddressed.[3,12] Deviations from nominal field dynamics arise primarily from low-pass behavior of gradient chains, delays, eddy currents,[13,14] and concomitant fields.[15] They may also involve anisotropic system response,[16] thermal drift,[17,18] and mechanical vibrations,[19] as well as dynamic susceptibility effects (e.g., caused by breathing)[20–22]. The chief traditional means of addressing these issues are delay calibration,[3] gradient pre-emphasis,[23] and measurement of effective k-space trajectories[3,24,25] for use in Fourier reconstruction. In recent years, dynamic field imperfections have also been tackled by concurrent field recordings and field models of higher spatial order.[26]

The second principal challenge in spiral imaging is static off-resonance, which arises from magnetic field nonuniformity and chemical shift. Off-resonance causes phase errors that scale with readout duration and are thus particularly limiting for single-shot acquisition.[3,12,27] When unaddressed, with spiral readouts they give rise to point spread function (PSF) broadening and thus to blurring in resulting images. This problem can be mitigated by parallel imaging with k-space undersampling and array detection,[28–32] although at the expense of SNR. At the reconstruction level, off-resonance is most commonly countered by conjugate-phase reconstruction, which works within certain limits on how rapidly frequency offsets may vary in space.[33–36] More general cases have been tackled with iterative reconstruction algorithms for full-Fourier encoding[37–39] and parallel imaging.[40] To address static and dynamic field perturbations jointly, image reconstruction has recently been performed by inversion of an expanded signal model, incorporating the encoding effects of both as well as those of array detection.[26]

Using an expanded signal model, single-shot spiral imaging with promising image quality has recently been reported for 3 T,[7,41] achieving 1.3-mm in-plane resolution in the brain with readouts of 32 ms. Such readout specifications are suited for diffusion imaging and BOLD fMRI at intermediate field strength and voxel size. However, single-shot readouts are equally attractive at higher main field and resolution, particularly for BOLD fMRI and ASL, which benefit greatly from enhanced baseline sensitivity.[42,43] At 7 T, spiral imaging has only been reported with segmented readouts up to 20 ms, targeting structural contrast.[44,45] Toward single-shot high-resolution acquisition at 7 T, the main obstacle is that high field exacerbates the off-resonance challenge. Higher fields tend to be less uniform, as susceptibility effects scale with field strength. Additionally, off-resonance phase accrual increases as readouts grow longer for higher resolution.

The purpose of the present work is to take on this challenge and explore the feasibility of single-shot spiral acquisition at high field. Brain imaging with T_2^* contrast is performed at 7 T using the expanded-model approach for reconstruction. Single-shot 2D imaging is accomplished with 0.8-mm nominal in-plane resolution, relying on extended readouts of 53 ms in length. In addition, long-readout capability is deployed for dual-image acquisition with successive inward and outward spirals.

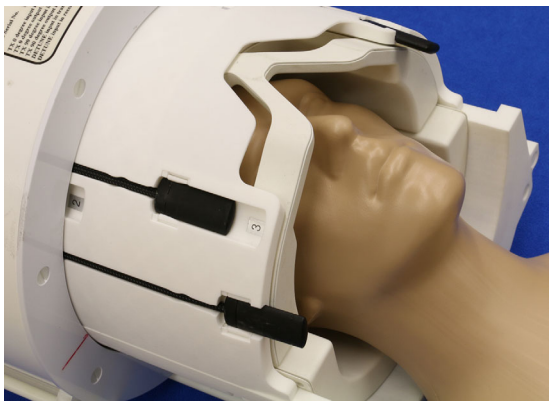

FIGURE 1 Setup for concurrent field monitoring: NMR field probes (black) are placed at suitable positions between the receive array and the surrounding transmitter, which slides over the receive part for operation

2 | METHODS

2.1 | Setup

All experiments were carried out on a 7 T Achieva system (Philips Healthcare, Best, Netherlands) using a quadrature-transmit and 32-channel head receive array (Nova Medical, Wilmington, MA). The system was operated in a mode offering a maximum gradient amplitude of 31 mT/m at maximum slew rate of 200 T/m/s on all axes simultaneously. For field recordings, an array of 16 fluorine NMR field probes (hexafluorobenzene, $T_1 = 86$ ms, $T_2^* = 24$ ms) [3,46–48] were integrated in the head setup. The probes were mounted on a laser-sintered nylon frame between the transmit coil and the receive array (Figure 1). The probe positions on the frame were determined by joint minimization of RF interaction with the volume transmitter and noise propagation from probe signals into spherical harmonic field expansions. At a droplet diameter of 800 μm, the probes were suitable for k-space excursions up to the equivalent of 400-μm resolution. The field-recording setup was operated with the transmit/receive chains and console hardware described in Ref 49. Data were collected from healthy volunteers according to the applicable ethics regulation.

2.2 | Spiral sequences

Archimedean spiral readouts were incorporated in a multislice 2D gradient-echo sequence (Figure 2). The spiral gradient waveforms were computed so as to minimize their duration within gradient-strength and slew-rate constraints.[50]

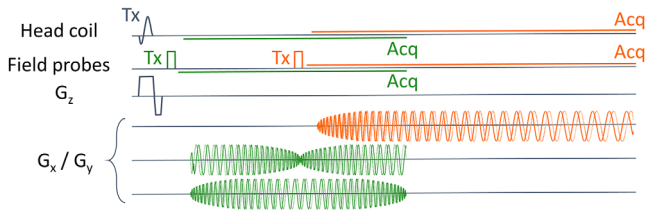

FIGURE 2 Diagram of the gradient-echo sequences used in this work. Orange: single-shot spiral-out acquisition. Green: spiral-in-out and spiral-out-in trajectories that read out two images successively ("half-shot"). Solid and dashed lines plot G_x and G_y, respectively. Field probes are excited before the respective spiral waveform and then read out concurrently with head-coil acquisition

The radial spacing of spiral turns was set so as to undersample k-space by a factor of 4 with respect to the FOV of 23 cm. Upon repetition, each trajectory was rotated by increments of 90° such that 4 successive acquisitions jointly amounted to full Fourier sampling. Table 1 lists further parameters of 3 specific trajectory implementations sketched in Figure 2. The first of these, targeting high resolution, was a center-out spiral with a nominal in-plane resolution of 0.8 mm (35 spiral revolutions per shot) used to read out slices of 1-mm and 2-mm thickness. In the second and third examples, lower-resolution (1.5 mm in-plane, 2-mm slices, 20 spiral revolutions per half-shot) outward and inward spirals were concatenated in either order, forming spiral-in-out and spiral-out-in schemes. Acquiring 2 images after a single excitation, these readouts are also referred to as *half-shot* spirals in the following. In the spiral-in-out case, a suitable prephasing gradient was included before the inward part. Throughout, slice excitation was preceded by a SPIR (Spectral Presaturation with Inversion Recovery) module[51] to suppress fat signal from the scalp (not shown in the sequence diagram). The whole brain was covered by 36 equidistant, transverse slices, resulting in a slice repetition time of 3.3 seconds.

TABLE 1 Sequence parameters

Readout trajectory	Spiral-out	Spiral-in-out	Spiral-out-in
Resolution (mm)	0.8	1.5	1.5
FOV (cm)	23	23	23
Undersampling factor R	4	4	4
TE (ms)	25	22/22	3/40
Readout time (ms)	53	2*18.5	2*18.5
Number of slices	36	36	36
Slice thickness (mm)	1, 2	2	2
Slice gap (mm)	2.5, 1.5	1.5	1.5

2.3 | Field recording

The field probes were excited just before the start of the spiral waveforms and read out concurrently with image acquisition (Figure 2). Field recording was performed for every third slice and interpolated for adjacent slices, allowing near-complete probe recovery between excitations. The phase time courses of acquired probe signals were used to calculate a time-resolved field expansion in terms of second-order spherical harmonics.[25] Second-order concomitant field effects were estimated based on the dominant first-order harmonics.[15] The probe phase time courses were then corrected for the estimated concomitant field contributions before refitting the harmonic model.[41]

2.4 | Image reconstruction

Image reconstruction was based on the expanded signal model detailed in Refs 7 and 26. In the absence of diffusion gradients, higher-order eddy-current effects were assumed to be negligible as previously observed in Ref 45 for the same system. The resulting first-order model reads

$$s_\gamma(t) = \int_V m(\boldsymbol{r})\, e^{i(k_0(t)+\boldsymbol{k}(t)\cdot\boldsymbol{r})}\, e^{i\Delta\omega_0(\boldsymbol{r})\,t}\, c_\gamma(\boldsymbol{r})\, dV \qquad (1)$$

with static frequency offset $\Delta\omega_0$, sensitivity c_γ and signal s_γ of coil γ, initial transverse magnetization m, and position vector $\boldsymbol{r} = [x\ y\ z]^T$ within the imaging volume V. k_0 and $\boldsymbol{k} = [k_x\ k_y\ k_z]^T$ describe phase accrual due to zeroth-order and first-order components of the recorded dynamic field expansion.

Discretization of space and time according to the targeted resolution and the acquisition bandwidth translates Equation 1 into

$$\tilde{s}_{(\gamma,\tau)} = \sum\nolimits_\rho E_{(\gamma,\tau),\rho}\, m_\rho, \qquad (2)$$

where the indices ρ and τ count voxels and sampling time points, respectively; $m_\rho = m(\boldsymbol{r}_\rho)$; and E denotes the encoding matrix with entries

$$E_{(\gamma,\tau),\rho} = e^{i\boldsymbol{k}(t_\tau)\cdot(\boldsymbol{r}_\rho-\boldsymbol{r}_0)}\, e^{i\Delta\omega_0(\boldsymbol{r}_\rho)\,t_\tau}\, c_\gamma(\boldsymbol{r}_\rho). \qquad (3)$$

In this notation, geared to 2D imaging, zeroth-order field and gradients orthogonal to the image plane are accounted for by initial signal demodulation as follows:

$$\tilde{s}_{(\gamma,\tau)} = e^{-i\,(k_0(t_\tau)+\boldsymbol{k}(t_\tau)\cdot\boldsymbol{r}_0)}\, s_{(\gamma,\tau)} \qquad (4)$$

where $s_{(\gamma,\tau)} = s_\gamma(t_\tau)$ and $\boldsymbol{r}_0$ points to the center of the slice and FOV. In matrix-vector form, the signal model then reads

$$\tilde{\boldsymbol{s}} = E\,\boldsymbol{m}. \qquad (5)$$

Inversion of Equation 5 is performed by conjugate-gradient (CG) iteration.[28] Matrix-vector multiplications in the CG loop were accelerated by use of fast Fourier transform enabled by forward and reverse gridding[28] and

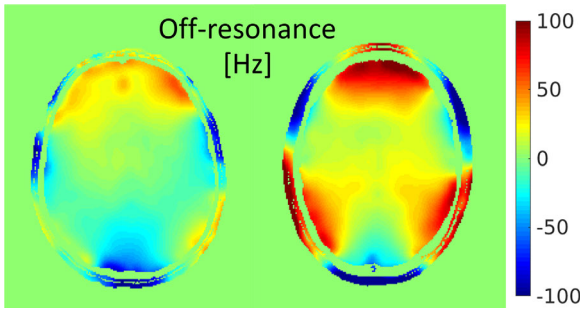

FIGURE 3 Off-resonance maps for central slices. Left: first subject (Figures 4 and 6). Right: second subject (Figures 8 and 9)

multiple-frequency interpolation.[7,36,40] Image reconstruction was performed on a 32-node central processing unit (CPU) cluster using MATLAB (The MathWorks, Natick, MA) and critical routines implemented in C.

Maps of $\Delta\omega_0$ (Figure 3) and coil sensitivity were calculated from a separate fat-suppressed Cartesian gradient-echo scan with full Fourier encoding and multiple echoes. The Cartesian gradient-echo images were reconstructed in the same way as described previously, although neglecting off-resonance and coil sensitivity. The former was negligible because of the large bandwidth of the Cartesian gradient-echo scan. Ignoring coil sensitivity resulted in separate sensitivity-weighted images per receive coil. Raw $\Delta\omega_0$ maps were obtained by pixel-wise fitting of phase evolution over the different TEs. Coil sensitivity maps were obtained from the first-echo data, dividing single-coil images by the root-sum-of-squares across the array. Both types of maps were refined by smoothing and slight extrapolation using a variational approach, penalizing roughness along with deviations from the original.[52] In reconstructed images, residual weighting by net array sensitivity was removed by bias field correction (SPM12, http://www.fil.ion.ucl.ac.uk/spm/software/spm12/), which is based on an automatic segmentation approach detailed in Ref 53.

To study the effect of the different encoding terms in the signal model, the high-resolution spiral-out data were also reconstructed based on the nominal dynamic field evolution ($k_0(t)=0$, nominal k-space trajectory) and/or neglecting off-resonance. To illustrate the effect of parallel imaging, single-shot results are compared with reconstruction from fully Fourier-encoded data obtained with four shots.

2.5 | PSF analysis

T_2^* decay during center-out spiral readouts reduces spatial resolution by radial signal attenuation in k-space. To assess the extent of this effect, the PSF was determined for single-shot spiral-out acquisitions based on the high-resolution trajectory specified previously. In addition to the full trajectory of 53 ms, fragments of length between 10 and 50 ms were created by truncation, using 5-ms increments. The PSFs were obtained by emulating signal acquisition and image reconstruction for a point source at the center of the FOV. Array signals from a point source were synthesized by Equation 1 and then attenuated by T_2^* decay. T_2^* values were taken from Ref 54, which reports 33.2 ms (gray matter) and 26.8 ms (white matter) for human brain at 7 T. Reconstruction was performed as described previously, yielding PSFs on the image grid. For PSF analysis, the spatial representation was refined by a factor of 10 in both dimensions, using zero-padding in the Fourier domain.

3 | RESULTS

3.1 | Single-shot spirals

Figure 4 shows the results of the high-resolution study, yielding single-shot images of 0.8-mm nominal resolution based on readouts of 53 ms each. In the top panel, 5 selected slices of the data set with 2-mm slice thickness are displayed. Based on spiral-out trajectories starting at a TE of 25 ms, the data exhibit T_2^* contrast similar to typical acquisitions in BOLD fMRI. Sharp delineation of tissue borders is achieved, particularly between gray and white matter, as well as between brain parenchyma and CSF. Notably, the obtained images do not exhibit the issues that have traditionally been associated with spiral imaging. Despite high field and very long readouts, they are not conspicuously blurred or distorted. In 2 slices, a hypo-intense feature is visible between the frontal lobes. This has been confirmed to reflect a calcification of the falx cerebri, a nonpathogenic variation within the healthy population that is equally visible in the Cartesian prescans. In the shown data, it caused intravoxel dephasing, which is a consequence of the long TE rather than the readout strategy. The corresponding results obtained with 1-mm slice thickness are shown in the second panel of Figure 4, along with smaller displays over a larger slice range. As expected, smaller voxel volume in these scans yields noticeably lower SNR. At the same time, the thinner slices appear slightly sharper, especially at gray and white matter and brain-CSF interfaces. Overall, high quality of depiction at still considerable SNR is accomplished in the thinner slices.

Figure 5 shows the underlying time courses of the recorded phase coefficients k_l for one slice. The zeroth-order coefficient is plotted in the top panel. The first-order coefficients in the middle reflect the common k-space trajectory. The bottom graph shows the second-order coefficients, which were neglected in image reconstruction.

The results of varying the signal model are displayed in Figure 6, based on 1-mm slices. The panel on the left compares the reconstructions from 4-shot, fully Fourier-encoded data, ignoring coil sensitivity in the signal model. Assuming nominal field evolution deteriorated the image quality substantially, mostly by blurring and general corruption of edges

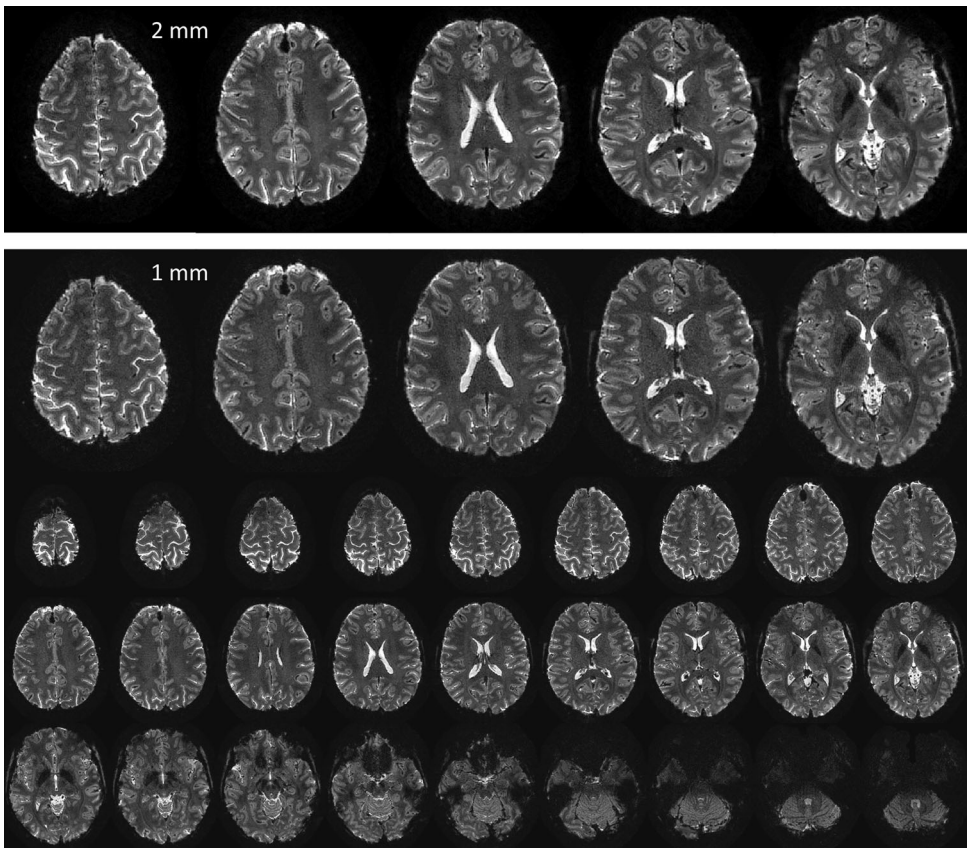

FIGURE 4 Spiral-out imaging with TE = 25 ms, 0.8-mm nominal resolution. The bottom panel displays the central 27 of 36 slices at 1-mm slice thickness. Five selected slices are shown magnified for closer inspection and comparison with thicker slices (2 mm)

and contours. The appearance of these artifacts changes very little after including off-resonance in the signal model. The effect of the latter is more apparent when relying on recorded field evolution. In this case, accounting for $\Delta\omega_0$ visibly counters typical off-resonance effects such as blurring, signal pile-up, and distortion, mostly in regions close to the surface where resonance offsets tend to be the largest. The benefit of accounting for coil sensitivity, finally, is illustrated by moving from full Fourier encoding to single-shot data with 4-fold undersampling and array reconstruction (Figure 6, right panel).

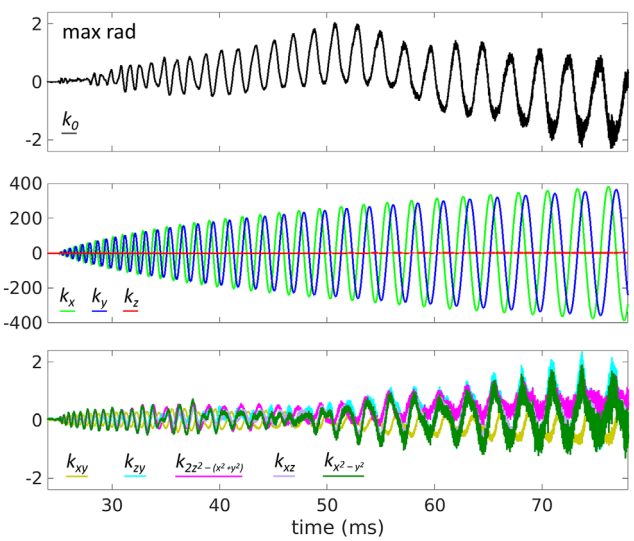

FIGURE 5 Monitored field dynamics in terms of ^{1}H phase accrual, expanded into spherical harmonics of zeroth-order to second-order (top to bottom). The first-order terms are the common k-space coordinates. Plots are scaled to show maximum phase excursion in [rad] within a sphere of 10-cm diameter. Note the different scaling of the vertical axis for the first-order terms (left)

The results of the PSF study are shown in Figure 7. As the acquisition duration increases, nominal resolution improves approximately as the inverse square root of acquisition time, reflecting the square dependence of the net k-space area on the k-space radius. At the level of PSFs, a convenient resolution metric is the FWHM, which is approximately 1.4 times the nominal resolution. Neglecting T_2^* decay, the FWHM reaches 1.12 mm at the full readout length of 53 ms, corresponding to 0.8-mm resolution. In gray and white matter, finite T_2^* causes the FWHM to improve more slowly, reaching 1.32 and 1.38 mm, respectively, which corresponds to resolutions of 0.94 and 0.98 mm. The benefit of increasing the readout duration further is reflected by the final slope of the FWHM plots. For gray and white matter, this slope is approximately two-thirds of that obtained without T_2^* decay. In CSF, T_2^* is much longer than the acquisition times considered here, and thus hardly impairs the nominal resolution.

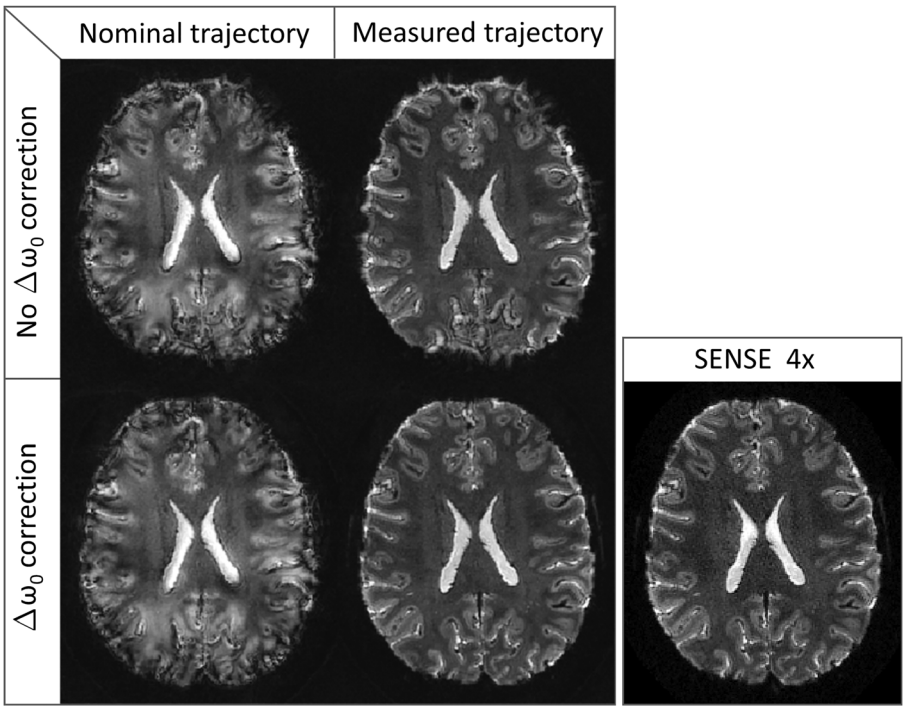

FIGURE 6 Effect of signal model constituents, shown for a 1-mm slice selected from Figure 4. The four images in the left panel were reconstructed from four successive spiral shots, amounting to full-density k-space sampling. Image reconstruction was performed with and without accounting for static and measured dynamic field as indicated. The right panel shows the single-shot case (4-times undersampling), relying on the coil sensitivity terms in the signal model in addition to $\Delta\omega_0$ (Figure 3, left) and the measured trajectory (Figure 5)

3.2 | Half-shot spirals

Figures 8 and 9 display the results of half-shot imaging, obtained by separate reconstruction from the inward and outward parts of the double spirals. Figure 8 shows spiral-in-out imaging, yielding two images per slice that exhibit similar contrast, as the subtrajectories visit the center of k-space at the same time. They differ somewhat in sharpness of contours, which the second spiral depicts blurrier around the scalp but sharper between CSF and white matter because of the long T_2^* of the former. The later acquisitions also exhibit stronger attenuation of residual fat signal and somewhat more pronounced signal dropout as a result of dephasing in voxels exposed to susceptibility gradients. Figure 9 shows the corresponding spiral-out-in results, which exhibit strongly distinct contrast caused by the discrepancy in TE (3 versus 40 ms). At the short TE, residual fat signal from the scalp gives rise to slight ringing. With the spiral-in readout, off-resonance correction still achieves good integrity of depiction despite very late acquisition of central k-space.

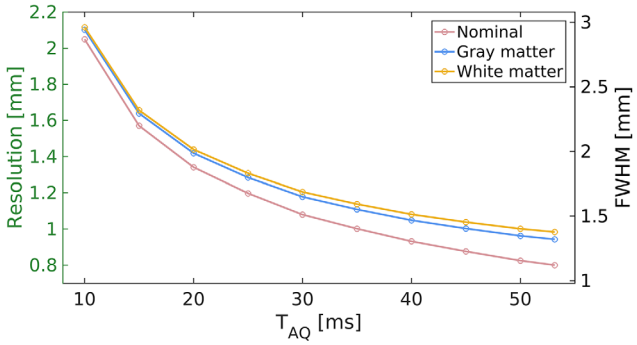

FIGURE 7 Effect of T_2^* decay on image resolution and the equivalent FWHM of the point spread function (PSF). Red: nominal resolution obtained with the single-shot spiral-out approach as a function of acquisition duration. Blue, yellow: actual resolution in the presence of T_2^* decay as encountered in gray and white matter, respectively

4 | DISCUSSION

The results of this study show that single-shot spiral acquisition is a viable means of boosting encoding speed for high-field brain imaging. Competitive image quality has been achieved by inversion of an expanded signal model that jointly accounts for static off-resonance, actual k-space trajectories, zeroth-order field dynamics, and sensitivity encoding with a receiver array. With this approach, extended readouts of 53 ms have been found to be robust at 7 T, encoding nominal in-plane resolution of 0.8 mm in a single shot. These specifications are remarkable in that they exceed those previously reported for spiral imaging at 3 T, despite worse B_0 uniformity at higher field.

Rapid high-resolution readouts leverage the SNR advantage of high field, which makes them attractive for a range of applications. Submillimeter resolution by single shots is especially attractive for BOLD fMRI time series. In this

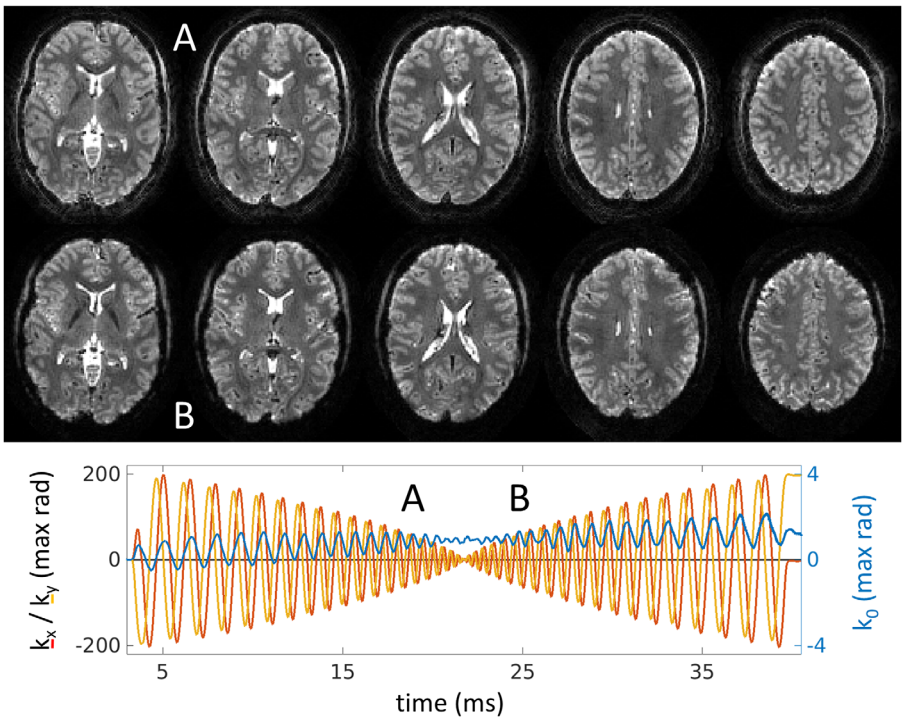

FIGURE 8 Spiral-in-out reconstruction results for 5 selected slices and the underlying recorded trajectory (zeroth and first order). A, Spiral-in images. B, spiral-out images

study, T_2^*-weighted data still featured visually appealing sensitivity even at 1-mm slice thickness, and thus at a sub-μL voxel volume. Another promising application is ASL, which typically targets somewhat lower resolution but benefits particularly from the combination of high acquisition duty cycle and the short TE that spirals offer. These features are equally desired in diffusion-weighted scanning, which is also increasingly explored at high field.[55,56]

As illustrated in the second part of this study, extended spiral readouts can also be used to acquire two images after a

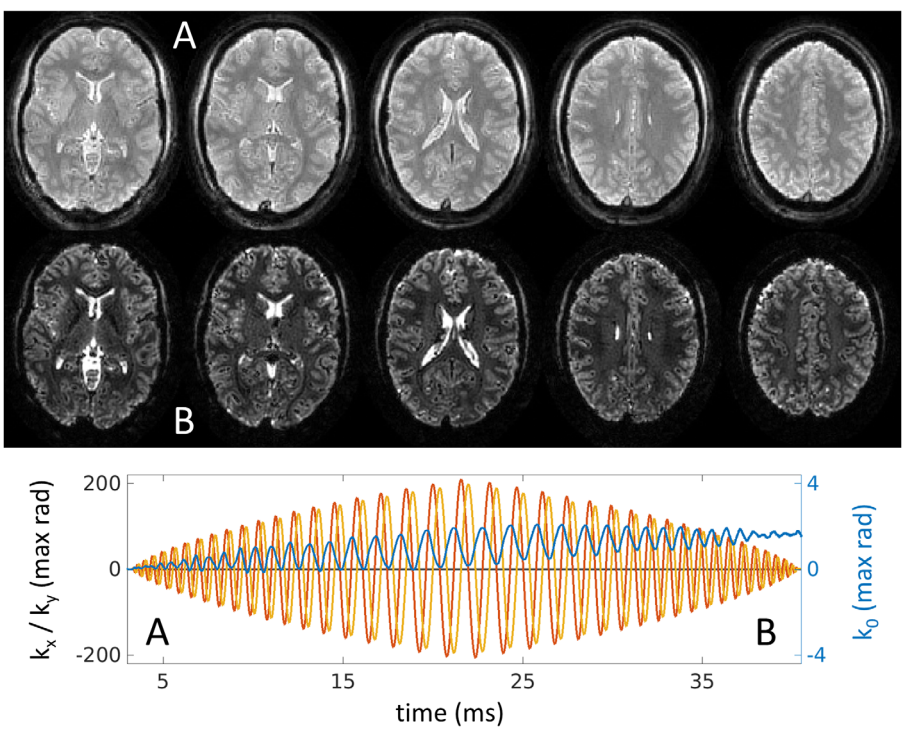

FIGURE 9 Spiral-out-in reconstruction results for 5 selected slices and the underlying recorded trajectory (zeroth and first order). A, Spiral-out images. B, spiral-in images

single excitation in what may be called a half-shot strategy. This approach was pioneered in fMRI, particularly for physiological noise correction[57] and multi-echo combination,[10,58] and has also been used for joint water-fat estimation.[59,60] Two successive spiral readouts may also be of different length and k-space range. In particular, a leading or trailing low-resolution spiral could serve for supporting purposes such as navigation or $\Delta\omega_0$ and coil sensitivity mapping. Finally, good quality of depiction with single-shot 2D spirals suggests that other long and non-Cartesian readouts, particularly 3D and multiband spirals,[59,61,62] may hold promise for similar levels of robustness.

As observed in the PSF study, T_2^* decay during the spiral readout causes actual resolution in gray and white matter to fall somewhat short of the nominal values. If considered limiting, this type of resolution loss could be countered at the raw data level by compensatory multiplication with the inverse of a decay exponential, assuming some intermediate global T_2^* value. With this approach, PSF broadening for short-T_2^* tissue will be mitigated, while oversharpening the PSF of long-T_2^* material, particularly of cerebrospinal fluid. Boosting attenuated data in this way must be done with moderation to limit the amplification also of noise and of PSF side lobes for long-T_2^* material, which will appear as ringing. Alternatively, when leaving the raw data uncompensated as done here, the T_2^* decay has the same effect as common ringing filters, which also attenuate PSF side lobes at some expense in resolution. Importantly, actual resolution in brain as a function of readout duration was found to still exhibit a significant slope at the reported acquisition time of 53 ms. This indicates that moving to readouts of such length does pay off in terms of resolution, and even somewhat longer acquisition may still add to image quality.

Good quality of depiction reflects the suitability of the signal model, and all constituents of the model have been found to be essential for the single-shot case (Figure 6). However, limitations to the model remain. Most prominently, in the form used here it does not describe intravoxel field variation. Therefore, in-plane and through-plane dephasing in regions with strong static field gradients remain unaddressed. This applies to the area of the ear canals, the orbits, the nasal cavities, and, in the case shown, to a calcification between the frontal lobes (Figure 4). Signal dropout may be countered partly by exciting thinner slices, yet at the expense of SNR. Enhancing the signal model toward intravoxel description is straightforward per se and an interesting option but will render the inverse problem ill-conditioned. With regard to readout strategies, it is important to note that dephasing issues are not specific to spiral scans, but rather inherent to long readout schemes.

Regardless of model-inherent constraints, depiction quality is also limited by the finite accuracy of the model ingredients. Strong local field variation introduces error also in $\Delta\omega_0$ mapping, which is manifest as residual blurring and distortion in the same critical regions as mentioned previously (lower slices in Figure 4). When disregarding $\Delta\omega_0$, similar artifacts appear to a greater extent and in all brain regions (Figure 6). The fidelity of $\Delta\omega_0$ and coil sensitivity maps is also impaired by motion between the mapping scan and subsequent spiral scans. The $\Delta\omega_0$ maps tend to be more critical in this respect. This is partly because of their finer structure, especially at the interfaces between brain tissue, skull, scalp, and air. In addition, off-resonance is caused mostly by tissue susceptibility, and thus changes strongly as the head moves. In contrast, coil sensitivity reflects primarily coil geometry and is influenced more indirectly by changes in load upon motion. When limiting, geometric congruency between different scans can generally be improved by motion tracking with navigators,[63] optical cameras,[64] or field probes.[65,66] However, because both susceptibility and RF effects are orientation-dependent, large motion will still be limiting. The need to map $\Delta\omega_0$ and coil sensitivity in the first place also takes additional time. In the present work, a robust, high-resolution scan of 5 minutes was used for this purpose and no effort was made to minimize the time burden. There is scope for reducing it, however, by faster imaging techniques and compromising on spatial resolution.

The third model ingredient, field dynamics, can be determined by a range of methods. Spiral trajectories have been mapped previously using additional reference scans on a phantom or the subject itself.[24,67–69] More recently they have also been predicted based on gradient impulse response functions.[41,70,71] In the present work, field dynamics were recorded with NMR probes, which is convenient in that it can be performed concurrently with actual imaging and will capture potential system drifts and other transient effects. In previous studies, magnet drift and heating of gradient coils have been identified as relevant system changes, giving rise to image variation up to several percent in EPI.[18,72] Differences between trajectory prediction based on impulse response and concurrent trajectory recording were also reported in Ref 41, resulting in RMS image differences of approximately 2% for single-shot spiral imaging.

While all imaging in this work was in transverse orientation, the field sensing and reconstruction approaches hold unaltered for arbitrary slice angulation.[41] The level of gradient fidelity and feasibility of correction at the reconstruction stage do not commonly vary greatly with slice geometry. However, differences in static off-resonance and through-plane gradients will cause some dependence of image quality on slice position and orientation. The relaxation times and droplet size of the field probes determine the feasible specifications of spiral readouts as well as the maximum rate of probe re-excitation. At a droplet diameter of 0.8 mm, the probes used here support imaging down to resolutions of approximately 0.4 mm,[25] which is amply sufficient for the

single-shot scenario. At the used probe T_2^* of 24 ms, probe readouts could not be extended much beyond the durations used in this work. Longer spiral acquisition could be readily supported, however, with probes doped for longer signal lifetime.

An important challenge that comes with expanding the signal model is increased computation for model inversion. Readout duration is a key determinant of reconstruction time, as it co-defines the number of frequency segments required for multiple frequency interpolation. For the longest readouts of 53 ms, reconstruction times ranged up to 10s of seconds per image. However, exploring feasibility, no efforts have been undertaken to render reconstruction particularly efficient. Toward routine use, there is substantial scope for acceleration by basic algorithmic optimization as well as distribution on ever larger CPU or GPU (graphics processing unit) clusters.[73]

CONFLICTS OF INTEREST

Klaas Pruessmann holds a research agreement with and receives research support from Philips Healthcare. Klaas Pruessmann is a shareholder of Gyrotools LLC and Skope Magnetic Resonance Technologies AG. Christoph Barmet and Bertram Wilm are shareholders of Skope Magnetic Resonance Technologies AG.

REFERENCES

[1] Ahn CB, Kim JH, Cho ZH. High-speed spiral-scan echo planar NMR Imaging-I. *IEEE Trans Med Imaging.* 1986;5:2-7.

[2] Meyer CH, Hu BS, Nishimura DG, Macovski A. Fast Spiral Coronary Artery Imaging. *Magn Reson Med.* 1992;28:202-213.

[3] Börnert P, Schomberg H, Aldefeld B, Groen J. Improvements in spiral MR imaging. *Magn Reson Mater Phys Biol Med.* 1999;9: 29-41.

[4] Glover GH, Lai S. Self-navigated spiral fMRI: Interleaved versus single-shot. *Magn Reson Med.* 1998;39:361-368.

[5] Nishimura DG, Irarrazabal P, Meyer CH. A Velocity k-Space analysis of flow effects in echo-planar and spiral imaging. *Magn Reson Med.* 1995;33:549-556.

[6] Liu C, Bammer R, Kim D, Moseley ME. Self-navigated interleaved spiral (SNAILS): Application to high-resolution diffusion tensor imaging. *Magn Reson Med.* 2004;52:1388-1396.

[7] Wilm BJ, Barmet C, Gross S, et al. Single-shot spiral imaging enabled by an expanded encoding model: Demonstration in diffusion MRI. *Magn Reson Med.* 2017;77:83-91.

[8] Meyer CH, Zhao L, Lustig M, et al. Dual-density and parallel spiral ASL for motion artifact reduction. In Proceedings of the 19th Annual Meeting of ISMRM, Montréal, Canada, 2011. p. 3986.

[9] Noll DC, Cohen JD, Meyer CH, Schneider W. Spiral K-space MR imaging of cortical activation. *J Magn Reson Imaging.* 1995;5:49-56.

[10] Glover GH, Law CS. Spiral-in/out BOLD fMRI for increased SNR and reduced susceptibility artifacts. *Magn Reson Med.* 2001;46:515-522.

[11] Jung Y, Samsonov AA, Liu TT, Buracas GT. High efficiency multishot interleaved spiral-in/out: Acquisition for high-resolution BOLD fMRI. *Magn Reson Med.* 2013;70:420-428.

[12] Block KT, Frahm J. Spiral imaging: A critical appraisal. *J Magn Reson Imaging.* 2005;21:657-668.

[13] Boesch C, Gruetter R, Martin E. Temporal and spatial analysis of fields generated by eddy currents in superconducting magnets: Optimization of corrections and quantitative characterization of magnet/gradient systems. *Magn Reson Med.* 1991;20:268-284.

[14] Liu Q, Hughes DG, Allen PS. Quantitative characterization of the eddy current fields in a 40-cm bore superconducting magnet. *Magn Reson Med.* 1994;31:73-76.

[15] Bernstein MA, Zhou XJ, Polzin JA, et al. Concomitant gradient terms in phase contrast MR: Analysis and correction. *Magn Reson Med.* 1998;39:300-308.

[16] Aldefeld B, Börnert P. Effects of gradient anisotropy in MRI. *Magn Reson Med.* 1998;39:606-614.

[17] Busch J, Vannesjo SJ, Barmet C, Pruessmann KP, Kozerke S. Analysis of temperature dependence of background phase errors in phase-contrast cardiovascular magnetic resonance. *J Cardiovasc Magn Reson.* 2014;16:97.

[18] Kasper L, Bollmann S, Vannesjo SJ, et al. Monitoring, analysis, and correction of magnetic field fluctuations in echo planar imaging time series: magnetic field fluctuations in EPI. *Magn Reson Med.* 2015;74:396-409.

[19] Wu Y, Chronik BA, Bowen C, Mechefske CK, Rutt BK. Gradient-induced acoustic and magnetic field fluctuations in a 4T whole-body MR imager. *Magn Reson Med.* 2000;44:532-536.

[20] Van de Moortele P-F, Pfeuffer J, Glover GH, Ugurbil K, Hu X. Respiration-induced B0 fluctuations and their spatial distribution in the human brain at 7 Tesla. *Magn Reson Med.* 2002;47:888-895.

[21] Versluis MJ, Peeters JM, van Rooden S, et al. Origin and reduction of motion and f0 artifacts in high resolution T2*-weighted magnetic resonance imaging: Application in Alzheimer's disease patients. *NeuroImage.* 2010;51:1082-1088.

[22] Vannesjo SJ, Wilm BJ, Duerst Y, et al. Retrospective correction of physiological field fluctuations in high-field brain MRI using concurrent field monitoring: Physiological field correction using concurrent field monitoring. *Magn Reson Med.* 2015;73:1833-1843.

[23] Morich MA, Lampman DA, Dannels WR, Goldie FTD. Exact temporal eddy current compensation in magnetic resonance imaging systems. *IEEE Trans Med Imaging.* 1988;7:247-254.

[24] Duyn JH, Yang Y, Frank JA, van der Veen JW. Simple Correction Method for k-Space Trajectory Deviations in MRI. *J Magn Reson.* 1998;132:150-153.

[25] Barmet C, Zanche ND, Pruessmann KP. Spatiotemporal magnetic field monitoring for MR. *Magn Reson Med.* 2008;60:187-197.

[26] Wilm BJ, Barmet C, Pavan M, Pruessmann KP. Higher order reconstruction for MRI in the presence of spatiotemporal field perturbations. *Magn. Reson. Med.* 2011;65:1690-1701.

[27] Yudilevich E, Stark H. Spiral sampling in magnetic resonance imaging - The effect of inhomogeneities. *IEEE Trans Med Imaging.* 1987;6:337-345.

[28] Pruessmann KP, Weiger M, Börnert P, Boesiger P. Advances in sensitivity encoding with arbitrary k-space trajectories. *Magn Reson Med.* 2001;46:638-651.

[29] Weiger M, Pruessmann KP, Österbauer R, Börnert P, Boesiger P, Jezzard P. Sensitivity-encoded single-shot spiral imaging for reduced susceptibility artifacts in BOLD fMRI. *Magn Reson Med.* 2002;48:860-866.

[30] Yeh EN, Stuber M, McKenzie CA, et al. Inherently self-calibrating non-Cartesian parallel imaging. *Magn Reson Med.* 2005;54:1-8.

[31] Heberlein K, Hu X. Auto-calibrated parallel spiral imaging. *Magn Reson Med.* 2006;55:619-625.

[32] Heidemann RM, Griswold MA, Seiberlich N, et al. Direct parallel image reconstructions for spiral trajectories using GRAPPA. *Magn Reson Med.* 2006;56:317-326.

[33] Maeda A, Sano K, Yokoyama T. Reconstruction by weighted correlation for MRI with time-varying gradients. *IEEE Trans Med Imaging.* 1988;7:26-31.

[34] Noll DC, Meyer CH, Pauly JM, Nishimura DG, Macovski A. A homogeneity correction method for magnetic resonance imaging with time-varying gradients. *IEEE Trans Med Imaging.* 1991;10:629-637.

[35] Noll DC, Pauly JM, Meyer CH, Nishimura DG, Macovski A. Deblurring for non-2D Fourier transform magnetic resonance imaging. *Magn Reson Med.* 1992;25:319-333.

[36] Man L-C, Pauly JM, Macovski A. Multifrequency interpolation for fast off-resonance correction. *Magn Reson Med.* 1997;37:785-792.

[37] Harshbarger TB, Twieg DB. Iterative reconstruction of single-shot spiral MRI with off resonance. *IEEE Trans Med Imaging.* 1999;18:196-205.

[38] Sutton BP, Noll DC, Fessler JA. Fast, iterative image reconstruction for MRI in the presence of field inhomogeneities. *IEEE Trans Med Imaging.* 2003;22:178-188.

[39] Barmet C, Tsao J, Pruessmann KP. Efficient iterative reconstruction for parallel MRI in strongly inhomogeneous B_0. In Proceedings of the 13th Annual Meeting of ISMRM, Miami Beach, FL, 2004. p 347.

[40] Barmet C, Tsao J, Pruessmann KP. Sensitivity encoding and B0 inhomogeneity - A simultaneous reconstruction approach. In Proceedings of the 14th Annual Meeting of ISMRM, Seattle, WA, 2005. p. 682.

[41] Vannesjo SJ, Graedel NN, Kasper L, et al. Image reconstruction using a gradient impulse response model for trajectory prediction. *Magn Reson Med.* 2016;76:45-58.

[42] Goense J, Bohraus Y, Logothetis NK. fMRI at high spatial resolution: implications for BOLD-Models. *Front Comput Neurosci.* 2016;10.

[43] Ivanov D, Gardumi A, Haast RAM, Pfeuffer J, Poser BA, Uludağ K. Comparison of 3T and 7T ASL techniques for concurrent functional perfusion and BOLD studies. *NeuroImage.* 2017;156:363-376.

[44] Qian Y, Zhao T, Hue Y-K, Ibrahim TS, Boada FE. High-resolution spiral imaging on a whole-body 7T scanner with minimized image blurring. *Magn Reson Med.* 2010;63:543-552.

[45] Kasper L, Engel M, Barmet C, et al. Rapid anatomical brain imaging using spiral acquisition and an expanded signal model. *NeuroImage.* 2017. https://doi.org/10.1016/j.neuroimage.2017.07.062.

[46] Mason GF, Harshbarger T, Hetherington HP, Zhang Y, Pohost GM, Twieg DB. A Method to measure arbitrary k-space trajectories for rapid MR imaging. *Magn Reson Med.* 1997;38:492-496.

[47] De Zanche N, Barmet C, Nordmeyer-Massner JA, Pruessmann KP. NMR probes for measuring magnetic fields and field dynamics in MR systems. *Magn Reson Med.* 2008;60:176-186.

[48] Gross S, Barmet C, Dietrich BE, Brunner DO, Schmid T, Pruessmann KP. Dynamic nuclear magnetic resonance field sensing with part-per-trillion resolution. *Nat Commun.* 2016;7:13702.

[49] Dietrich BE, Brunner DO, Wilm BJ, et al. A field camera for MR sequence monitoring and system analysis. *Magn Reson Med.* 2016;75:1831-1840.

[50] Lustig M, Kim S-J, Pauly JM. A fast method for designing time-optimal gradient waveforms for arbitrary k-space trajectories. *IEEE Trans Med Imaging.* 2008;27:866-873.

[51] Kaldoudi E, Williams SCR, Barker GJ, Tofts PS. A chemical shift selective inversion recovery sequence for fat-suppressed MRI: Theory and experimental validation. *Magn Reson Imaging.* 1993;11:341-355.

[52] Keeling SL, Bammer R. A variational approach to magnetic resonance coil sensitivity estimation. *Appl Math Comput.* 2004;158:359-388.

[53] Ashburner J, Friston KJ. Unified segmentation. *NeuroImage.* 2005;26:839-851.

[54] Peters AM, Brookes MJ, Hoogenraad FG, et al. T2* measurements in human brain at 1.5, 3 and 7 T. *Magn Reson Imaging.* 2007;25:748-753.

[55] Heidemann RM, Porter DA, Anwander A, et al. Diffusion imaging in humans at 7T using readout-segmented EPI and GRAPPA. *Magn Reson Med.* 2010;64:9-14.

[56] In M-H, Posnansky O, Speck O. PSF mapping-based correction of eddy-current-induced distortions in diffusion-weighted echo-planar imaging. *Magn Reson Med.* 2016;75:2055-2063.

[57] Kundu P, Inati SJ, Evans JW, Luh W-M, Bandettini PA. Differentiating BOLD and non-BOLD signals in fMRI time series using multi-echo EPI. *NeuroImage.* 2012;60:1759-1770.

[58] Glover GH, Thomason ME. Improved combination of spiral-in/out images for BOLD fMRI. *Magn Reson Med.* 2004;51:863-868.

[59] Li Z, Wang D, Robison RK, et al. Sliding-slab three-dimensional TSE imaging with a spiral-In/Out readout. *Magn Reson Med.* 2016;75:729-738.

[60] Wang D, Zwart NR, Li Z, Schär M, Pipe JG. Analytical three-point Dixon method: with applications for spiral water-fat imaging. *Magn Reson Med.* 2016;75:627-638.

[61] Zahneisen B, Poser BA, Ernst T, Stenger AV. Simultaneous multi-slice fMRI using spiral trajectories. *NeuroImage.* 2014;92:8-18.

[62] Zahneisen B, Poser BA, Ernst T, Stenger VA. Three-dimensional Fourier encoding of simultaneously excited slices: Generalized

acquisition and reconstruction framework. *Magn Reson Med.* 2014;71:2071-2081.

[63] Lee CC, Jack CR, Grimm RC, et al. Real-time adaptive motion correction in functional MRI. *Magn Reson Med.* 1996;36:436-444.

[64] Zaitsev M, Dold C, Sakas G, Hennig J, Speck O. Magnetic resonance imaging of freely moving objects: prospective real-time motion correction using an external optical motion tracking system. *NeuroImage.* 2006;31:1038-1050.

[65] Ooi MB, Krueger S, Thomas WJ, Swaminathan SV, Brown TR. Prospective real-time correction for arbitrary head motion using active markers. *Magn Reson Med.* 2009;62:943-954.

[66] Haeberlin M, Kasper L, Barmet C, et al. Real-time motion correction using gradient tones and head-mounted NMR field probes. *Magn Reson Med.* 2015;74:647-660.

[67] Alley MT, Glover GH, Pelc NJ. Gradient characterization using a Fourier-transform technique. *Magn Reson Med.* 1998;39:581-587.

[68] Tan H, Meyer CH. Estimation of k-space trajectories in spiral MRI. *Magn Reson Med.* 2009;61:1396-1404.

[69] Robison RK, Devaraj A, Pipe JG. Fast, simple gradient delay estimation for spiral MRI. *Magn Reson Med.* 2010;63:1683-1690.

[70] Addy NO, Wu HH, Nishimura DG. A Simple Method for MR Gradient System Characterization and k-Space Trajectory Estimation. *Magn Reson Med.* 2012;68:120-129.

[71] Vannesjo SJ, Haeberlin M, Kasper L, et al. Gradient system characterization by impulse response measurements with a dynamic field camera. *Magn Reson Med.* 2013;69:583-593.

[72] Bollmann S, Kasper L, Vannesjo SJ, et al. Analysis and correction of field fluctuations in fMRI data using field monitoring. *NeuroImage.* 2017;154:92-105.

[73] Xue H, Inati S, Sørensen TS, Kellman P, Hansen MS. Distributed MRI reconstruction using gadgetron-based cloud computing: Gadgetron C-Bud computing. *Magn Reson Med.* 2015;73:1015-1025.

How to cite this article: Engel M, Kasper L, Barmet C, Schmid T, Vionnet L, Wilm B, Pruessmann KP. Single-shot spiral imaging at 7 T. *Magn Reson Med.* 2018;80:1836–1846. https://doi.org/10.1002/mrm.27176